A numerical method for the study of fluidic thrust-vectoring

Michele Ferlauto[a] and Roberto Marsilio[*]

*Department of Mechanical and Aerospace Engineering, Politecnico di Torino,
Corso Duca degli Abruzzi, 24, 10129, Turin, Italy*

Abstract.   Thrust Vectoring is a dynamic feature that offers many benefits in terms of maneuverability and control effectiveness. Thrust vectoring capabilities make the satisfaction of take-off and landing requirements easier. Moreover, it can be a valuable control effector at low dynamic pressures, where traditional aerodynamic controls are less effective. A numerical investigation of Fluidic Thrust Vectoring (FTV) is completed to evaluate the use of fluidic injection to manipulate flow separation and cause thrust vectoring of the primary jet thrust. The methodology presented is general and can be used to study different techniques of fluidic thrust vectoring like shock-vector control, sonic-plane skewing and counterflow methods. For validation purposes the method will focus on the dual-throat nozzle concept. Internal nozzle performances and thrust vector angles were computed for several range of nozzle pressure ratios and fluidic injection flow rate. The numerical results obtained are compared with the analogues experimental data reported in the scientific literature. The model is integrated using a finite volume discretization of the compressible URANS equations coupled with a Spalart-Allmaras turbulence model. Second order accuracy in space and time is achieved using an ENO scheme.

Keywords: thrust vectoring; dual throat nozzles; computational fluid dynamics

1. Introduction

Thrust Vectoring is a dynamic feature that offers many benefits in terms of maneuverability and control effectiveness. Thrust vectoring capabilities make the satisfaction of take-off and landing requirements easier. It is a valuable control effector at low dynamic pressures, where traditional aerodynamic controls are less effective. Advantages are also expected for supersonic regime, where the use of thrust vectoring nozzles can allow for airframe configurations having lower sonic-boom signatures, Flamm *et al.* (2006). Additionally, thrust vectoring could increase conventional controls for some control power to trim the aircraft and thus reduce cruise trim drag, Balu *et al.* (1991).

Unlike mechanical thrust-vectoring that uses actuated hardware to vector the jet thrust, Fluid Thrust Vectoring (FTV) nozzles use a secondary jet to manipulate the primary air stream. With respect to mechanical thrust vectoring devices the FTV does not increase significantly the aircraft weight and can be also applied to systems that were not designed with such feature.

---

[*]Corresponding author, Associate Professor, E-mail: roberto.marsilio@polito.it
[a]Assistant Professor, E-mail: michele.ferlauto@polito.it

Some of the mechanisms for thrust vector control include shock-vector control, sonic-plane skewing and counterflow (Anderson *et al.* 1997, Flamm 1998). The shock-vector control method (injection downstream nozzle throat) offers substantial vector control but often reduces thrust ratio, Deree (2003). Sonic-plane skewing methods (injection at nozzle throat) produce higher thrust ratios but lower resultant thrust vector angles when compared with the shock-vector control method, Yangle *et al*. (2000). The counterflow method (suction in a secondary duct between a primary exhaust nozzle and an aft collar) generates large vector angles with little secondary flow requirements, but issues such as suction supply source, hysteresis effects and airframe integration need to be addressed, Flamm (1998).

Among different deflection strategies of the nozzle flow, we focused on the Dual-Throat Nozzle (DTN) concept investigated in Flamm *et al*. (2006). The nozzle concept, shown in Fig. 1(a), is a 2-D convergent-divergent-convergent nozzle with two geometric minimum area, "dual-throats". A cavity is formed between two geometric minimum areas. The injection slot is located at the upstream minimum area and the asymmetric injection of secondary flow creates a new pattern in the main stream. The sonic plane become skewed, vectoring the primary flow and forcing flow separation in the cavity located on the injection side. A recirculation bubble forms in the separated-flow cavity and the corresponding wall pressure is pumped down by the primary flow. The cavity on the opposite side of the injection slot is filled by the high-pressure primary flow. The low pressure in one cavity coupled with the high pressure in the opposite cavity further vector the flow. Therefore, thrust vectoring is further enhanced over the throat skewing alone concept by the presence of the cavity regions.

In recent studies (Flamm *et al.* 2006, Deere *et al.* 2007) many geometries and flow injection settings have been experimentally and numerically tested with this design, and up to 15 degrees of vectoring have been achieved with very low losses in nozzle efficiency. Other numerical investigations about FTV have been performed by different research groups testing new DTN settings and geometries, (Bellandi and Slippey 2009, Shin *et al.* 2010). Different nozzle concepts, (Eilers *et al.* 2012), and control strategies, (Gonzalez *et al.* 2015), have also been investigated. Focusing on the nozzle steady state configuration, the numerical method used for the simulation of FTV were mainly based on compressible flow solvers (in-house or commercial) using the $k - \epsilon$ or $k - \omega$ SST models and acceleration techniques.

In the present work, a numerical framework for the simulation of the unsteady evolution of the controlled nozzle system is presented. The fully unsteady RANS equations are integrated by using a parallel finite volume approach with second order accuracy in both time and space. The code was developed with particular attention to the unsteady simulation of flow control problems (Ferlauto and Marsilio 2014) where separated flow are simulated and unsteadiness, turbulence modelling and compressibility effects may affect the final solution. As a validation for the proposed flow device, the numerical results about steady configurations at different flow injection rates and nozzle pressure ratios are compared with the experimental and numerical data available in literature.

2. Governing equations

The main flow field is simulated using a finite volume discretization of the unsteady Reynolds-averaged Navier-Stokes equations (URANS). The one-equation model of Spalart-Allmaras (S-A), (Spalart and Allmaras (1994)), is used for the turbulence modeling.

(a) Sketch of dual throat nozzle   (b) Geometry of dual throat nozzle
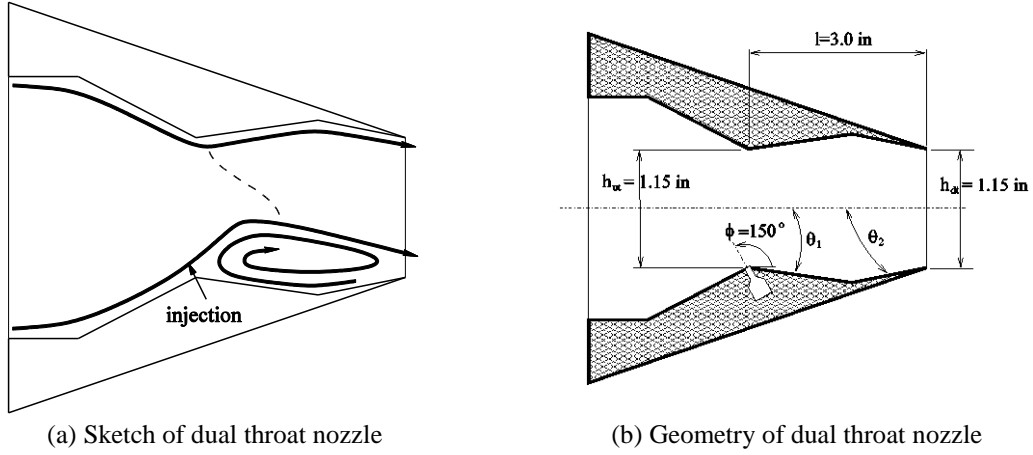
Fig. 1 Dual throat fluidic thrust vectoring nozzle

The set of governing equations are written in the compact integral form

$$\frac{\partial}{\partial t}\int_v \vec{W}dv + \int_S \vec{F}_I \cdot \vec{n}dS + \int_S \vec{F}_v \cdot \vec{n}dS = \int_v \vec{H}\,dv \qquad (2)$$

where v represents an arbitrary volume enclosed in a surface S. $\vec{W}$ is the hyper-vector of conservative variables, $\vec{F}_I$ and $\vec{F}_v$ are the tensors containing the inviscid and the viscous fluxes, respectively.

$$
\begin{aligned}
\vec{W} &= \{\rho, \rho\vec{q}, E, \tilde{\nu}_t\}^T \\
\vec{F}_I &= \{\rho\vec{q}, p\bar{\bar{I}} + \rho\vec{q}\otimes\rho\vec{q}, (E+p)\vec{q}, \tilde{\nu}_t\vec{q}\}^T \\
\vec{F}_v &= \frac{\sqrt{\gamma M_\infty}}{Re_\infty}\left\{0, -\bar{\bar{\tau}}, -\kappa\nabla T - \bar{\bar{\tau}}\cdot\vec{q}, -\frac{\nu+\tilde{\nu}_t}{\sigma}\nabla\tilde{\nu}_t\right\}^T
\end{aligned}
\qquad (3)
$$

Quantities ρ, p and $\vec{q} = \{u, v, w\}$ are the local density, pressure and the velocity vector, respectively; E is the total energy per unit volume, M_∞ and Re_∞ are the free-stream Mach number and the Reynolds number, γ is the ratio of the specific heats and finally $\bar{\bar{I}}$ is the unit matrix. The non-homogeneous term $\vec{H}$ is due to the turbulence model:

$$\vec{H} = \left\{0,0,0, c_{b1}\tilde{S}\tilde{\nu}_t + \frac{c_{b2}}{\sigma}(\nabla\tilde{\nu}_t)^2 - c_{w1}f_w\left(\frac{\tilde{\nu}_t}{d}\right)^2\right\}^T \qquad (4)$$

Turbulent eddy viscosity $\tilde{\nu}_t$ contains turbulence model constants and parameters. The reader is referred to Spalart and Allmaras (1994) for a full explanation of the model and constants. System (2) is non-dimensionalzed with respect to the reference length, L_{ref}, to free-stream density ρ_∞, temperature T_∞ and viscosity μ_∞.

The viscous stresses are written as

$$\tau_{ij} = (\mu + \mu_t)\left\{\frac{\partial q_j}{\partial x_i} + \frac{\partial q_i}{\partial x_j} - \frac{2}{3}(\nabla\cdot\vec{q})\delta_{ij}\right\} \qquad (5)$$

where δ_{ij} is the Kroneker's symbol and the laminar viscosity μ is computed via Sutherland's law. The turbulent viscosity $\mu_t = \rho\nu_t$ is computed through the Spalart-Allmaras one-equation

turbulence model (Spalart and Allmaras 1994). The integration in time is carried out according to a 4th Runge Kutta scheme and according to an Essentially Non-Oscillatory (ENO) scheme second order accurate in both time and space. Moreover, the numerical code has the capability to simulate time-varying boundary conditions. Details of the computational numerical study can be found in Ferlauto and Marsilio (2006) and Ferlauto and Marsilio (2014). Solution are deemed converged when thrust vector angle varied less than 0.5° over several thousand iterations. Solution residuals were monitored and a drop of at least 2 orders of magnitude was obtained for the solution to be considered converged. The numerical method has been efficiently parallelized by using OpenMP directives. The Spalart-Allmaras turbulence model has been selected after a survey of the literature on the numerical simulation of SJ flow fields by URANS solvers. The spatial and time-accuracy of the core solver we used has been widely tested in many unsteady simulation of compressible flowfields as: flow manipulation and post-stall control of NACA0015; unsteady supersonic combustion, (Ferrat and Marsilio 2012); in simulating time-dependent flows with moving grids, aeroelastic computations, blade flutter analysis and for the simulation of rotating stall generation and evolution, (Ferlauto and Rosa Taddei 2015).

2.1 Model description

The experimental model used in Flamm *et al.* (2006) is a 2-D convergent-divergent-convergent nozzle with two geometric minimum areas. A cavity between the two minimum areas is also included. The nozzle wide was 4.0 in. The upstream and downstream nominal throat heights were $h_{ut} = h_{dt} = 1.5$ in. The nominal upstream and downstream throat areas were 4.6 sq. in. Fig. 1(b) shows a sketch of the model illustrating the geometric design variables used to obtain the experimental results. The cavity length test was $l = 3.0$ in. In Flamm *et al.* (2006) different divergent, θ_1, and convergent, θ_2, cavity ramp angles and different injection geometries were tested. The secondary flow was injected at the upstream minimum area, (see Fig. 2(b)).

In this paper, for validation purpose, the case corresponding to $\theta_1 = -10$ and $\theta_2 = 20$ degrees and using a slot as injection geometry has been analyzed. The slot injector had a total open area of 0.0864 square inches. The secondary flow injection angle, ϕ was 150 degrees for all configuration used.

2.2 Computational domain and boundary conditions

The numerical simulations were carried out using 2-D computational structured grids. The different grids are generated by an in-house conformal mapping grid generator tool. The computational mesh modeled an injection slot angled at 150° upstream. The mesh was appropriately stretched to ensure a sufficient number of grid points on the injection slot.

Boundary conditions have been imposed following the guidelines of Poinsot and Lele (1992). Nozzle walls were simulated with adiabatic, no-slip boundary conditions for viscous effects. The nozzle inlet conditions were set with a total temperature and a total pressure boundary condition. Riemann invariants along the characteristics were used for upstream, upper and lower far field boundary conditions. A subsonic, constant pressure outflow boundary condition, which switches to supersonic boundary condition if the flow Mach number is supersonic, was used along the downstream far field boundary. Fig. 2(a) shows the computational domain with the different boundary conditions, BC, imposed.

The injection flow was simulated using inlet boundary conditions applied to the jet slot situated

(a) View of the computational domain (b) Direction and position of the secondary jet
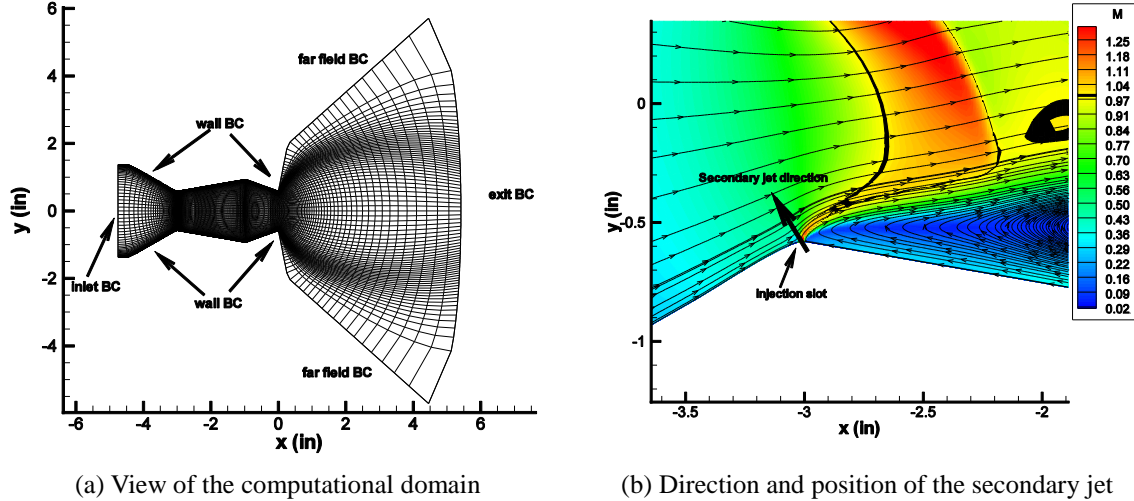
Fig. 2 Dual throat nozzle computational domain and boundary conditions

in the lower part of the nozzle wall close to the throat. For the injection flow boundary conditions the total temperature and the total pressure were imposed so as to guarantee the right amount of the ejected mass flow. In Fig. 2(b) the secondary jet zone is shown together with the computed Mach number and relative streamlines.

Different grid sizes were also used to evaluate grid convergence and solution consistency. Solutions were run on coarse, medium and fine meshes.

3. Numerical results

In order to validate the numerical method the geometric nozzle configuration with $\theta_1 = -10^o$ and $\theta_2 = 20^o$ has been chosen. In Flam *et al.* (2006), Deere *et al.* (2005) the experimental data on the dual throat nozzle were acquired using static freestream conditions. Likewise, the computational solutions were simulated with a static freestream, although a small convective Mach number of $M_\infty = 0.01$ was used for computational stability. Moreover the following reference values: $L_{ref} = l = 3$ in., $T_\infty = 288.16$ K, $p_\infty = 101325$ Pa, were used for the computations.

The nozzle was operating at different pressure ratio, NPR, where NPR is the ratio of the inlet total pressure, p_t, over the discharge ambient pressure, p_a, $NPR = p_t/p_a$. The nozzle internal performances can be defined in terms of the resultant pitch thrust vector angle, $\delta_p = \tan^{-1} F_N/F_A$, of the discharge coefficient of primary nozzle, $C_d = (w_p + w_s)/w_{ip}$, and the resultant pitch thrust vectoring efficiency, η defined as

$$\eta = \frac{\delta_p}{\frac{w_s}{w_s+w_p}*100} \quad (6)$$

where F_N, F_A, w_s, w_p and w_{ip} are the nozzle normal force, the nozzle axial force, the weight flow rate of the secondary jet, the weight flow rate of the primary nozzle and the ideal weight flow rate

(a) Pitch thrust angle, δ_p, comparison

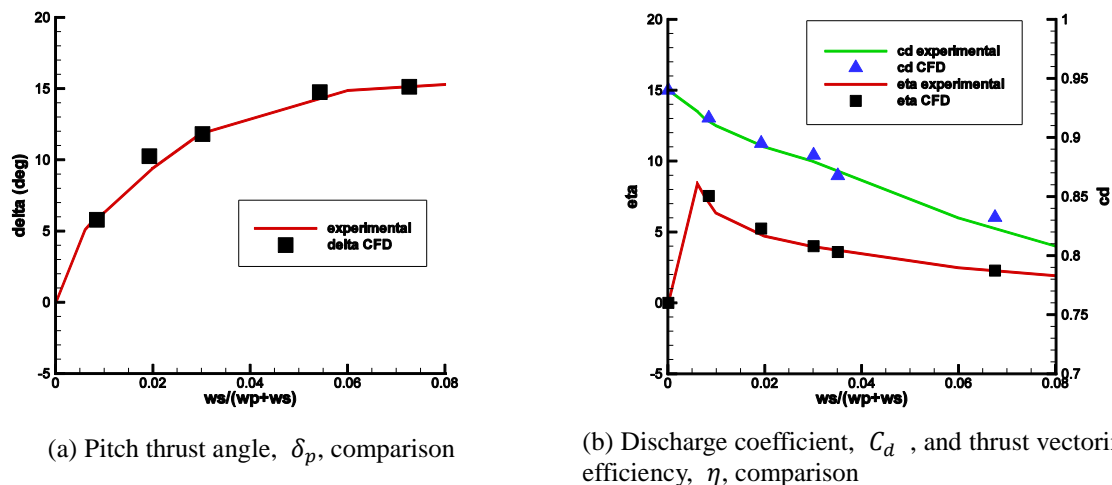(b) Discharge coefficient, C_d, and thrust vectoring efficiency, η, comparison

Fig. 3 Nozzle performance as function of the secondary weight-flow ratio at NPR=4.0

of the primary nozzle, respectively.
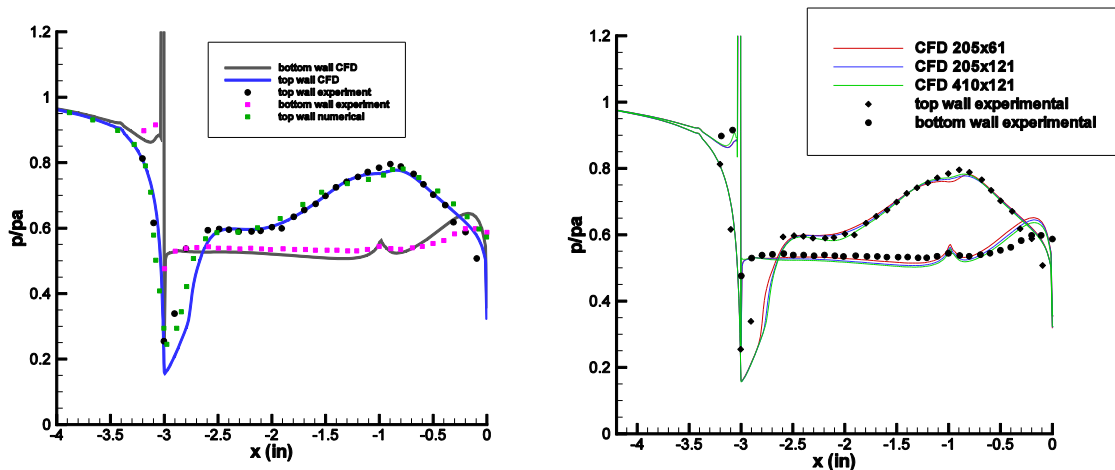
3.1 Nozzle performances at constant NPR

Fig. 3(a)-(b) show the comparison between the numerical computed, on a 205×121 points grid, and the experimental results reported in Flamm *et al.* (2006), in terms of the nozzle internal performances (δ_p, C_d, η) as a function of the secondary weight-flow, w_s, at NPR=4.0. In very good agreement with experimental data presented in Flemm *et al.* (2006), computational results verify that increasing the secondary weight flow ratio significantly increases the resultant pitch thrust angle δ_p. At NPR=4 an increment of the weight flow ratio from 2% to 7% the resultant pitch thrust angle increased from $\delta_p = 10.1^\circ$ to $\delta_p = 15.3^\circ$, Fig. 3(a), while the thrust vectoring efficiency, η decreases from 5 to 3 degree per cent secondary injection, Fig. 3(b). The discharge coefficient, C_d, follows similar trend decreasing with increasing secondary injection rate. Fig. 3 shows that all the numerical computed nozzle performances in terms of δ_p, C_d and η compare quite well with the experimental data reported in Flemm *et al.* (2006).

A comparison of the experimental pressure data measured over the walls of the primary nozzle with the computational prediction for 3% injection and NPR=4 is shown in Fig. 4(a). As expected from the good agreement shown in Fig. 3, the numerical and the experimental pressure data are remarkably similar for the configuration studied. The numerical method here presented was effective in predicting the flow characteristics along the upper wall with the shock very close to the exact location of the experiment. The upper surface distribution indicates lower pressure just downstream of the first throat ($x = -3$ in.) and higher pressure in the upper cavity. Moreover, the code was also been able to predict close enough the low pressure in the separated flow region along the lower wall. The curve is flat where the flow is separated along the cavity wall, and there is a slight increase in pressure near the nozzle exit as the primary jet vectors down and impinges on the lower surface.

A grid-refinement study has also been performed to evaluate grid convergence and solution consistency. Solutions were tested on three different grid sizes (205×61, 205×121, $410 \times$
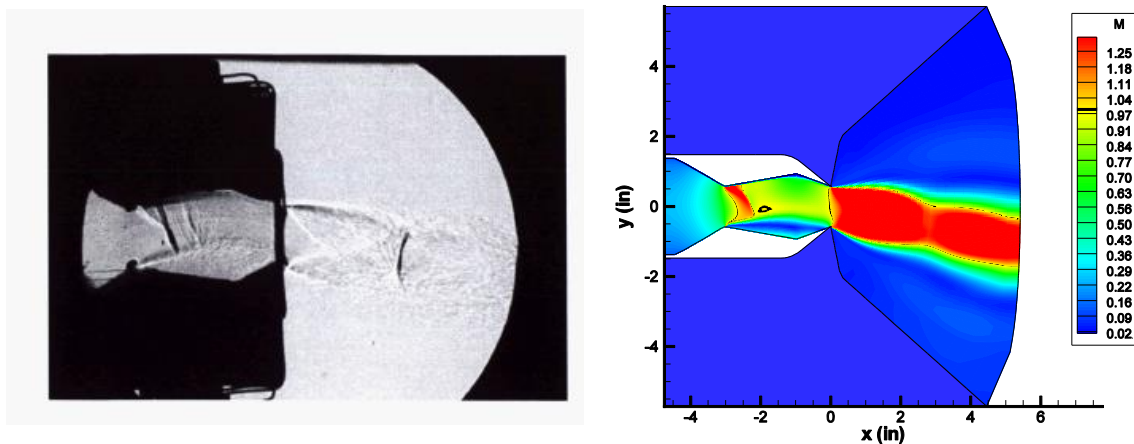
121 points) showing very small changes in internal nozzle performance parameters and thrust vector angles, with a good agreement in terms of wall pressure distribution, (see Fig. 4(b)). The medium mesh (205 × 121 points) was deemed more than sufficient for estimating performance trends and adequate for predicting performance magnitudes.

Fig. 5 presents an experimental shadowgraph image (from Flamm *et al.* (2006)) and computational Mach contours for the case in study. The computational flow pattern, Fig. 5(b), is in agreement with the experimental in terms of waves and topology flow characteristics. Moreover, in Fig. 5(b) are clearly visible the lambda foot on the upper divergent cavity wall with a strong shock to subsonic flow, flow separation in the upper cavity apex, massive flow separation along the lower cavity walls, and plume flow expansion to supersonic flow.

(a) Static pressure comparison   (b) Static pressure on different meshes

Fig. 4 Nozzle flow field at the deflected condition with 3% flow injection and NPR=4.0.

(a) Experimental shadowgraph (Flamm *et al.* 2006)   (b) Numerical Mach contour lines

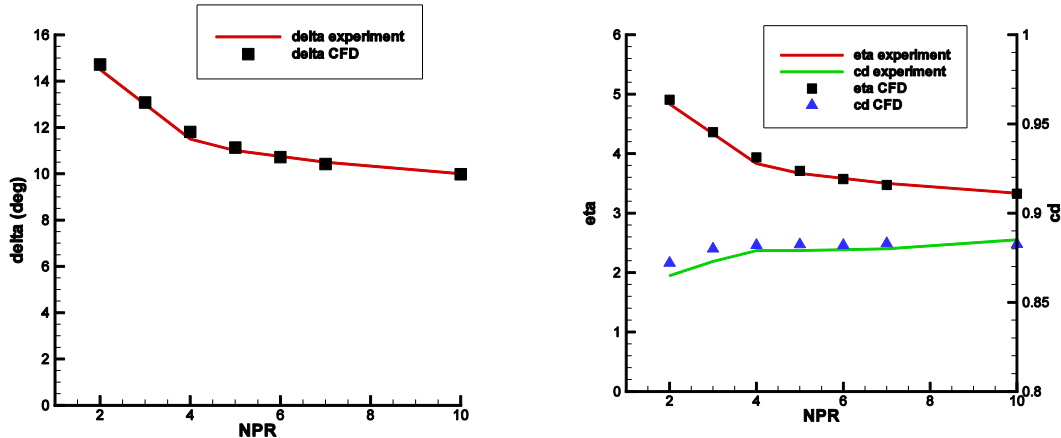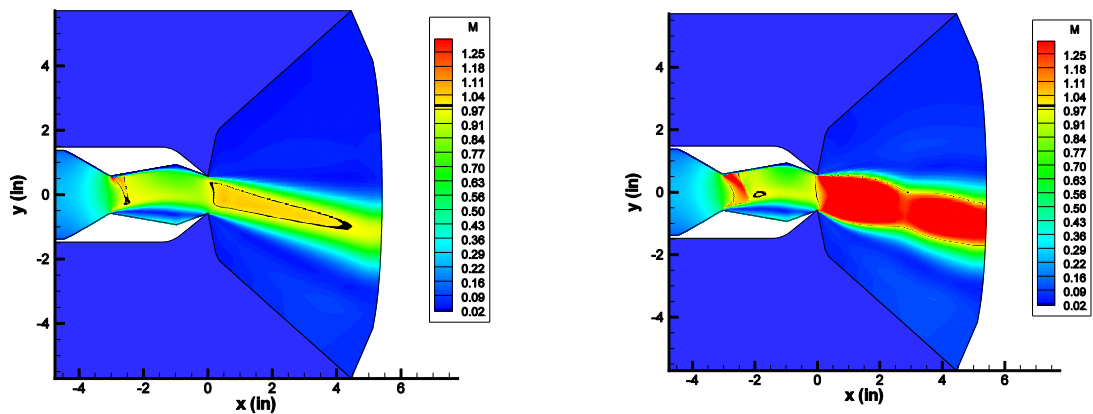Fig. 5 Nozzle flow field at the deflected condition with 3% flow injection and NPR=4.0

(a) Pitch thrust angle, δ_p, 3% injection

(b) Discharge coefficient, C_d, and thrust vectoring efficiency, η, 3% injection

Fig. 6 Nozzle performance as function of NPR at 3% injection

(a) Mach number at NPR=2, 3% injection

(b) Mach number at NPR=4, 3% injection

Fig. 7 Mach number contours at different NPR with 3% injection

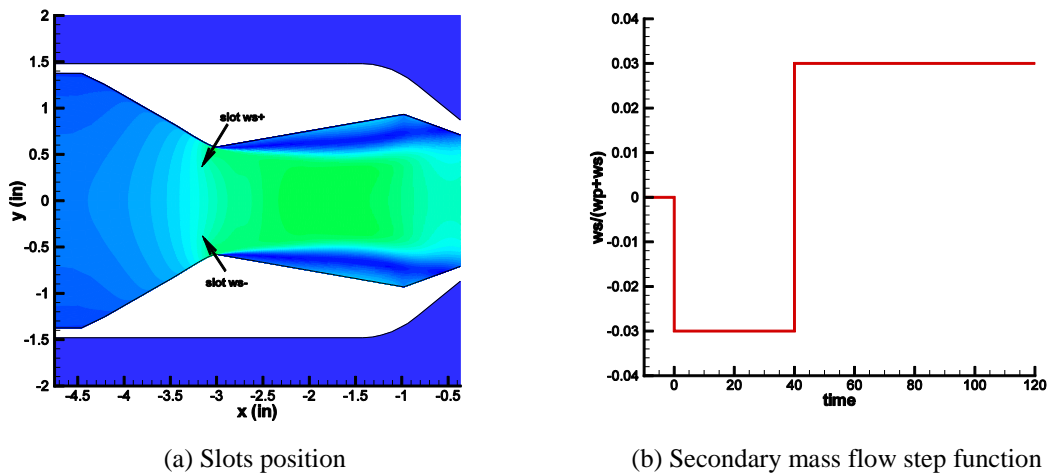## 3.2 Nozzle performances at different NPR

Simulations of the present nozzle geometric configuration operating at different NPR values (varying from 2 to 10) with 3% injection were also performed to complete the validation process. The comparison of the predicted results with the experimental data (Deere *et al.* 2005) for discharge coefficient and thrust vector angle are shown in Fig. 6. The pitch thrust vector angle and the thrust efficiency are predicted very well by the simulations over the entire range of NPR tested. Discharge coefficient was also predicted accurately, with small error at NPR≥4. Computational results indicated a higher discharge coefficient at NPR=2 than demonstrated experimental, which indicate less flow separation. The fluidic thrust vectoring using the dual-throat nozzle concept relies on separation in the recessed cavity to create a large pressure differential between the upper

and lower walls to vector the primary jet. Therefore, the magnitude of the thrust vector angle and discharge coefficient are strongly dependent by the turbulence model used. The higher discharge coefficient relative to experiment suggests that computational results predicted a smaller total pressure loss, at the nozzle exit, due to the separated turbulent flow in the lower cavity. The other differences that may results in minor discrepancies between experimental and computational data include differences between the experimental hardware and the modeled computational domain. In Fig. 7 the flow patterns in terms of Mach number contours for NPR=2, (Fig. 7(a)), and for NPR=4, (Fig. 7(b)), are shown. Increasing the NPR had a negative impact on the thrust vector angle, δ_p, and thrust vectoring efficiency, η. Discharge coefficient, C_d, increases very slightly with the increased of the NPR values. The effect of increasing NPR values are apparent in Fig. 7, which shows the effect of the NPR on Mach contours: first a downstream movement of the internal shock towards the nozzle exit and, second, increased flow separation on the nozzle upper cavity that results in a loss of discharge coefficient.

3.3 Unsteady simulations

The proposed method can be used for active control of the nozzle thrust vectoring. More specifically, it is possible to use the methodology to achieve a low-order dynamic model able to calculate the off-design performance of a jet engine with thrust vectoring capabilities. In this paper an example of the computational unsteady simulation is described. In Fig. 9 the time-response of the flow pattern to a step input function based on the secondary weight-flow at NPR=4, (see Fig. 8(b)), is shown. Two injection slots were positioned in the throat of the primary nozzle, one on the lower wall (slot ws-) and the other on the upper wall (slot ws+), Fig 8(a). The time variable shown in Fig. 8(b) and in Fig. 9 is the no-dimensional time unit where 1 unit corresponds to $8.85 \cdot 10^{-5}$ physical seconds.

At time < 0, the slots are both closed and no secondary flow is injected in the primary nozzle. The solution is symmetric without thrust vectoring, the pitch thrust vector angle $\delta_p = 0^o$, (Fig. 9(a)). At time = 0, the lower slot is instantly open while the upper slot remains close, the secondary

(a) Slots position   (b) Secondary mass flow step function

Fig. 8 Slots position and mass flow function for unsteady simulation at NPR=4
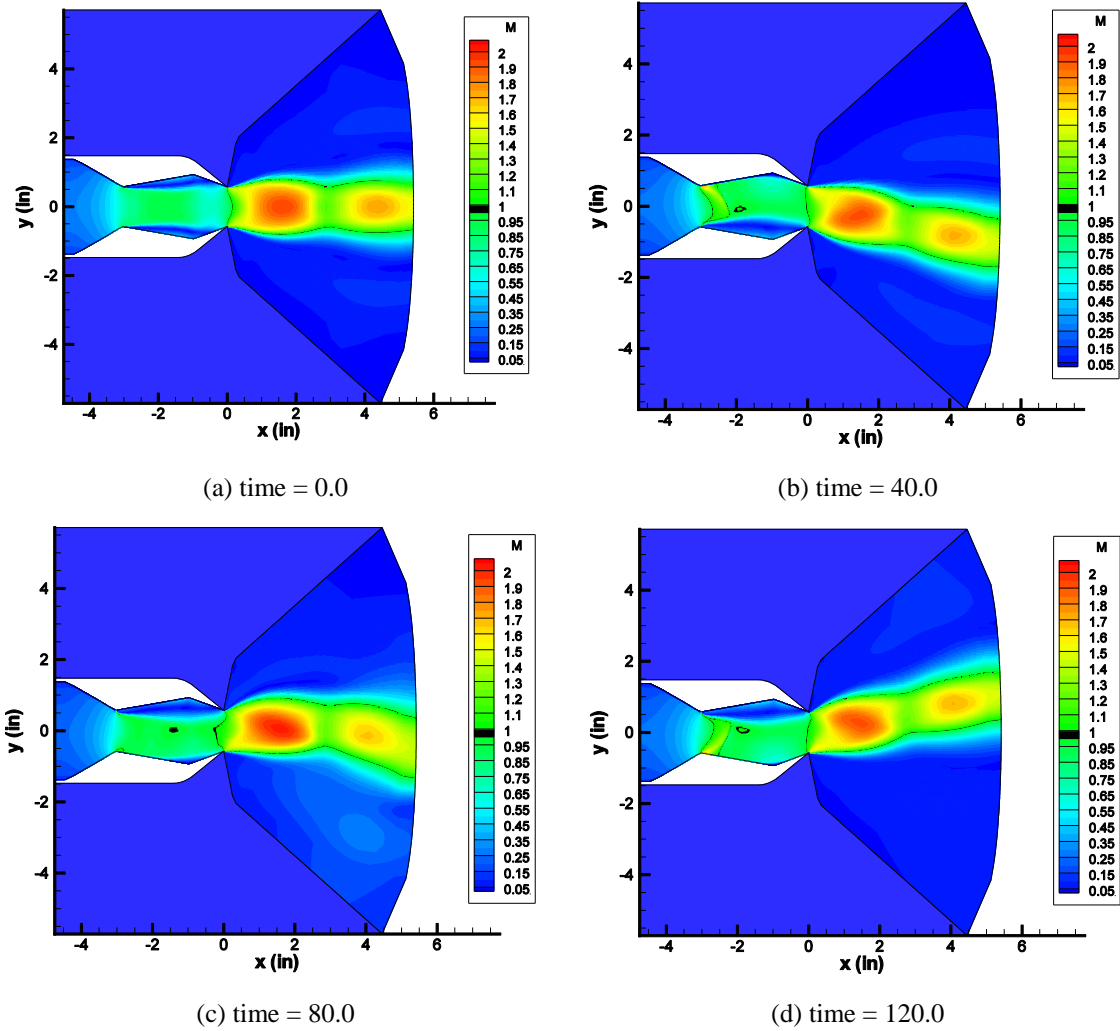
(a) time = 0.0

(b) time = 40.0

(c) time = 80.0

(d) time = 120.0

Fig. 9 Mach field evolution snapshots

flow is immediately injected with a direction $\phi = 150^{\circ}$ and 3% mass flow, $w_s/(w_p + w_s) = -0.03$. The solution reaches the steady state configuration a time = 40, with $\delta_p = -11.8^{\circ}$, (Fig. 9(b)). Negative and positive values of w_s and δ_p correspond to the secondary jet positioned on the lower and on the upper wall of the primary nozzle, respectively. At time = 40 the lower slot will be closed and the upper slot is instantly opened to permit, again, the injection of the secondary flow with $\phi = 150^{\circ}$ and 3% mass flow, $w_s/(w_p + w_s) = 0.03$. The steady state configuration is reached for time = 120, with $\delta_p = 11.8^{\circ}$, (Fig. 9(d)). So, as a response to a time-step function based on the secondary mass flow, in about 80 time units (about 7.08 milliseconds in physical time) the configuration is able to completely invert the thrust direction.

4. Conclusions

A computational tool for the investigation of FTV strategy has been presented. Fluid Thrust Vectoring uses fluidic injection to manipulate the flow separation inside the fixed nozzle and to cause asymmetric wall pressure distribution and, therefore, thrust vectoring. The numerical method has been validated for the complex case of the supersonic DTN tested at NASA LaRC, Deere *et al.* (2006).

The concept combines the thrust efficiency of sonic-plane skewing with increased thrust-vectoring efficiencies obtained by maximizing pressure differentials in a separated cavity located downstream of the nozzle throat. By injecting secondary flow asymmetrically at the upstream minimum area, a new aerodynamic minimum area is formed downstream of the geometric minimum and the sonic line is skewed, thus vectoring the exhaust flow.

An extensively analysis and validation has been carried-out in order to develop a numerical code that can predict the nozzle thrust-vectoring performances for control purposes. The numerical results obtained have shown a very good agreement with the experimental data published in the open literature for a wide range of nozzle pressure ratio and secondary flow injection rate.

The numerical method presented is also suitable for the extensive analysis of the nozzle control. As an example, the simulation of the DTN thrust vectoring in a closed-loop has been briefly illustrated.

Acknowledgements

References

Anderson, C.J., Giuliano, V.J. and Wing, D.J. (1997), "Investigation of hybrid fluidic / mechanical thrust vectoring for fixed-exit exhaust nozzles", *AIAA Paper, 97-3148*.

Balu, A.G., Marathe, P.J. and Mukunda, H.S. (1991), "Analysis of performance of a hot gas injection thrust vector control system", *J. Propuls. Power*, **7**, 580-585.

Bellandi, E. and Slippey, A. (2009), "Preliminary analysis and design enhancements of a dual-throat FTV nozzle concept", *39th AIAA Fluid Dynamics Conference*, AIAA Paper 2009-3900, San Antonio, Texas.

Deere, K.A., Flamm, J.D., Berrier, B.L. and Johnson, S.K. (2005), "A computational study of new dual throat thrust vectoring nozzle concept", *41st AIAA/ASME/SAE/ASEE Joint Propulsion Conference & Exhibit*, AIAA Paper 2005-3502.

Deere, K.A., Flamm, J.D., Berrier, B.L. and Johnson, S.K. (2007), "Computational study of an axisymmetric dual throat fluidic thrust vectoring nozzle for a supersonic aircraft application", *43rd AIAA/ASME/SAE/ASEE Joint Propulsion Conference & Exhibit*, AIAA Paper 2007-5085.

Deere, K.A. (2003), "Summary of fluidic thrust vectoring research conducted at NASA Langley Research Center", *AIAA Paper*, 2003-2800.

Eilers, S., Wilson, M., Whitmore, S. and Peterson, Z. (2012), "Side force amplification on an aerodynamically thrust vectored aerospike nozzle", *J. Propuls. Power*, **28**(4), 811-819.

Ferlauto, M. and Marsilio, R. (2001), "Computation of plug nozzle turbulent flowfields", *15th ISOABE Conference*, ISABE Paper-1185.

Ferlauto, M. and Marsilio, R. (2006), "A viscous inverse method for aerodynamic design", *Comput. Fluid.*, **35**, 304-325.

Ferlauto, M. and Marsilio, R. (2014), "A computational approach to the simulation of controlled flows by synthetic jets actuators", *Adv. Aircraft Spacecraft Sci.*, **2**(1), 77-94.

Ferlauto, M. and Rosa Taddei, S. (2015), "Reduced order modelling of full-span rotating stall for the flow control simulation of axial compressors", *Proceedings of the Institution of Mechanical Engineering Part A: Journal of Power and Energy*, **229**(4), 359-366.

Ferrat, C. and Marsilio, R. (2012), "A computational method for combustion in high speed flows", *Comput. Fluid.*, **70**, 44-52.

Flamm, J.D. (1998), "Experimental study of a nozzle using fluidic counterflow for thrust vectoring", *AIAA Paper*, 98-3255.

Flamm, J.D., Deere, K.A., Mason, M.L., Berrier, B.L. and Johnson, S.K. (2006), "Design enhancements of the two-dimensional, dual throat vectoring nozzle concept", *3rd AIAA Flow Control Conference*, San Francisco, CA, USA.

Gonzalez, D., Gaitondeb, D. and Lewisc, M. (2015), "Large-eddy simulations of plasma-based asymmetric control of supersonic round jets", *J. Comput. Fluid Dyn.*, **29**(3-5), 240-256.

Poinsot, T. and Lele, S. (1992), "Boundary conditions for direct simulations of compressible viscous reacting flows", *J. Comput. Phys.*, **101**, 104-129.

Shin, C., Kim, H., Setoguchi, T. and Matsuo, S. (2010), "A computational study of thrust vectoring control using dual throat nozzle", *J. Therm. Sci.*, **19**(6), 486-490.

Spalart, P. and Allmaras, S. (1994), "A one-equation turbulence model for aerodynamic flows", *La Recherce Aerospatiale*, **1**, 5-21.

Yangle, P.J., Miller, D.N., Ginn, K.B. and Hamstra, J.W. (2000), "Demonstration of fluidic throat skewing for thrust vectoring in structurally fixed nozzles", 2000-GT-0013, May 8-11.

EC